

# Performance Characterization of a Miniature, High Sensitivity Gamma Ray Camera

Peter D. Olcott, *Member, IEEE*, Frezghie Habte, *Member, IEEE*, Angela M. Foudray, *Student Member, IEEE*, and Craig S. Levin, *Member, IEEE*

**Abstract**—A compact, hand-held gamma camera with excellent intrinsic and extrinsic performance has been developed for the rapid identification and localization of sentinel lymph nodes during the surgical staging of cancer. The camera comprises a  $5 \times 5 \text{ cm}^2$  field of view NaI (TI) pixellated crystal array, a high sensitivity lead (2.0 cm thick) hexagonal parallel-hole collimator, a position sensitive photomultiplier tube (PSPMT), and a novel highly multiplexed electrical readout. The intrinsic energy resolution ( $12.1 \pm 2.0\%$ ) at 140 keV including edge crystals, extrinsic sensitivity ( $5 \text{ cps}/\mu\text{Ci}$  from 1–5 cm with a 24% energy window) and extrinsic spatial resolution ( $1.81 \pm 0.1 \text{ mm}$  at 0.6 cm) facilitate rapid identification of a radioactive node. Using a node phantom we performed an ideal observer study to estimate the detectability of small spheres in the range of 3 mm to 8 mm with different exposure times. With a 5 seconds exposure the camera can detect a 3 mm diameter sphere at a depth of 3.6 cm containing  $1 \mu\text{Ci}$  of Tc-99m within a cold background, and a 4 mm diameter sphere containing  $2 \mu\text{Ci}$  at 2.6 cm depth within a warm background ( $>10:1$  contrast) with a 5 second exposure duration.

**Index Terms**—Camera technology, detectors, mammotomography, miniature radiation cameras, Monte Carlo simulation, NMIS, PET instrumentation, SPECT instrumentation, x-ray CT instrumentation.

## I. INTRODUCTION

COMPACT hand-held gamma cameras may potentially be used to help localize the sentinel node in breast or skin cancer staging biopsy when used by itself or to augment a non-imaging counting probe procedure [1]. The sentinel lymph node (SLN) is defined as the first lymph node that drains the primary tumor basin. The SLN can be mapped by using a sulphur-colloid radiotracer labeled with Tc-99m that is injected near the primary tumor. Approximately  $500 \mu\text{Ci}$  to 1 mCi of tracer is injected near the primary tumor, with  $100 \text{ nCi}$  to  $2 \mu\text{Ci}$  of activity accumulating in the sentinel lymph nodes after it drains through the lymphatic channels [2]–[7]. Most of the activity stays within the injection site. In this paper, we describe the characterization of intrinsic and extrinsic performance of a small hand-held gamma camera we are

Manuscript received November 16, 2006; revised February 5, 2007. This work was supported in part by the Whitaker Foundation under Grant RG-01-0492.

P. D. Olcott, C. S. Levin, and A. M. Foudray are with the Department of Radiology, Molecular Imaging Program, Stanford University, Stanford, CA 94305 USA (e-mail: cslevin@stanford.edu).

F. Habte was with the Department of Radiology, Stanford University, Stanford, CA 94305 USA. He is now with the Science and Technology Division, Oak Ridge National Laboratory, Oak Ridge, TN 37831-6010 USA.

Digital Object Identifier 10.1109/TNS.2007.902367

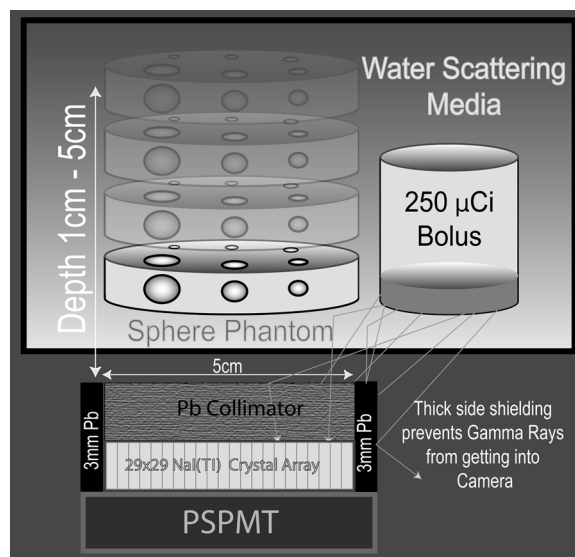


Fig. 1. The sphere phantom was placed at different depths in a water tank scattering medium. A 5 mL bottle with  $250 \mu\text{Ci}$  of Tc-99m was placed adjacent to the phantom just outside the field of view and within the tank to simulate the injection site. The spheres were 3–8 mm dia. filled with  $64 \mu\text{Ci}/\text{cc}$  Tc-99m water, with the smallest sphere containing approximately  $1 \mu\text{Ci}$ .

developing for sentinel lymph node imaging during melanoma and breast cancer staging. We also performed an observer study to evaluate the capabilities of the camera to detect small spheres at different depths in a water scattering medium.

## II. MATERIALS

The hand-held gamma camera consists of a  $5 \text{ cm} \times 5 \text{ cm} \times 2 \text{ cm}$  thick hexagonal parallel hole collimator with 1.3 mm hole size and 0.2 mm septa ( $5 \text{ cps}/\mu\text{Ci}$ ) coupled to a  $29 \times 29$  pixellated NaI(Tl) scintillation crystal array with a  $1.5 \text{ mm} \times 1.5 \text{ mm} \times 6 \text{ mm}$  individual crystal size and 1.7 mm pitch coupled to a flat panel, multi-anode Hamamatsu H8500 Position Sensitive Photomultiplier (PSPMT). The PSPMT is read out using a Symmetric Charge Division PCB Circuit [8]. Approximately 3 mm of lead shielding was wrapped around the collimator and the scintillation crystal. The node phantom consisted of small spheres ranging in size from 3 mm to 8 mm in diameter arranged in a circular pattern in a Lucite disk (Fig. 1).

## III. METHODS

### A. Intrinsic Camera Performance

The intrinsic energy gated flood image of the crystal array is generated by calculating and plotting the centroid of the 2-D

light distribution for each gamma ray interaction within the scintillation crystal resulting from Co-57 (122 keV) flood irradiation. After segmenting the 2-D flood histogram, event positions are assigned to individual crystals. The properties of each crystal that are of interest are the photopeak location, the photopeak energy resolution, and the photopeak counts.

Intrinsic spatial resolution is measured by stepping a collimated beam (0.6 mm FWHM) of Co-57 gamma rays across the face of the scintillation crystal (without a collimator). Events are binned to individual crystals and plotted as a function of known source location. The FWHM of the resulting trapezoid response function determines the intrinsic spatial resolution of the array. The counts in neighboring crystals give an indication of inter-crystal scatter, light diffusion, and unrelated background events.

### B. Extrinsic Camera Performance

We measured the sensitivity (the number of counts recorded per second/ $\mu\text{Ci}$ ) and the collimated spatial resolution (FWHM of the point spread function (PSF)), as a function of depth and collimator thickness. The extrinsic performance was measured with several collimators of varying thickness (0.5 cm–2 cm) and a 67  $\mu\text{Ci}$  Co-57 point source (0.5 mm diameter). The point source was stepped at several distances from the collimator and the sensitivity and resolution were extracted from the PSFs.

### C. Ideal Observer Using Sphere Phantoms

We chose to determine the efficacy of a hand-held camera for sentinel node detection by asking the question: In what fraction of frames acquired with a given exposure duration (acquisition time) do we correctly detect (true-positive) a sphere for different conditions such as node size, node depth, background contamination, and exposure duration using a-priori knowledge of the probably distribution functions for the spheres? This fraction can be estimated by performing an ideal observer study using the theory of signal detectability [10].

A simulation of the sentinel node environment was made using sphere phantoms submerged in water and placed next to a bottle filled with 250  $\mu\text{Ci}$  of Tc-99m in a 5 mL volume (see Fig. 1). The spheres were filled with a concentration of 64  $\mu\text{Ci}/\text{cc}$  Tc-99m aqueous solution. The activity per sphere ranged from approximately 1  $\mu\text{Ci}$  for the 3 mm to 16  $\mu\text{Ci}$  for the 8 mm diameter sphere. The potential for contamination from the injection site was simulated by using a 1:250 ratio of total activity of the smallest sphere to the total activity in the bottle. The bottle is only being used to simulate the potential but unlikely contamination from the injection site, and therefore, the total activity is important. A very weak warm background activity of 120  $\mu\text{Ci}$  was added to the 500 mL water tank to simulate the potential contamination from tissues, or lymph channels that could occur during a surgical staging procedure using sulphur-colloid.

Simulated frames of different exposure durations (0.5–5 seconds) were derived from a single 120-second acquisition taken for each sphere phantom at different depths and with different background contamination concentrations. A region of interest was drawn around each known sphere location. The counts per sphere per synthesized frame were histogrammed. The lambda

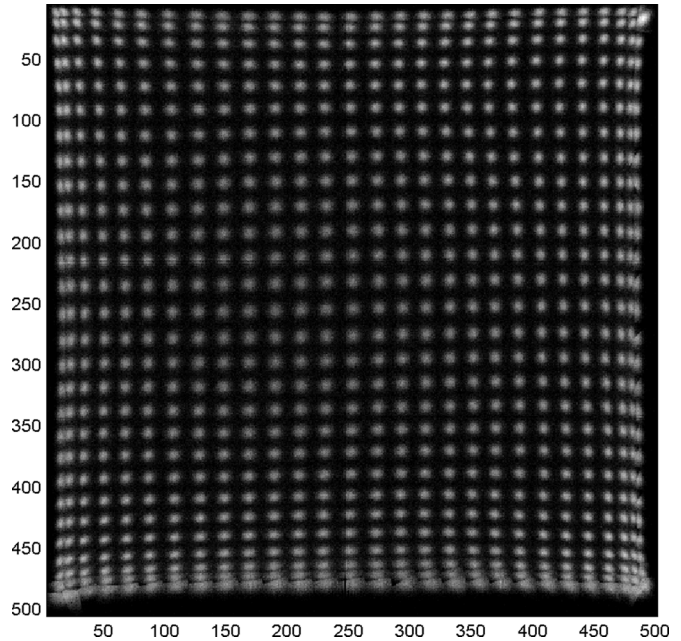


Fig. 2. Intrinsic per crystal energy gated 2-D flood histogram for a 10  $\mu\text{Ci}$  Co-57 point source flood irradiation at 30 cm distance. 27  $\times$  27 crystals are resolved out of a 29  $\times$  29 array of 1.5  $\times$  1.5  $\times$  6 mm<sup>3</sup> NaI(Tl) crystals.

parameter of a Poisson distribution was estimated from the normalized histogram of the counts per region of interest per frame. A minimum size of 9 pixels (approximately 5 mm in size) was used as the minimum background ROI and was scaled up to match larger sphere areas projected onto the camera.

The percentage of frames that detect a true positive sphere was estimated by comparing the lambda parameter of a Poisson distribution for the sphere at a given sphere size, depth, and exposure duration versus the background of equivalent area by choosing the statistically optimal (the ideal observer) decision threshold that minimizes the false positive and false negative probabilities.

### D. Image Processing

We developed real time image processing software and algorithms [9] to improve the visualization of the low count statistical images of gamma camera imaging. We apply 3x3 Gaussian smoothing, 8x bi-cubic interpolation, and non-linear image compression to bring out low intensity regions while at the same time suppressing extremely high intensity regions.

## IV. RESULTS

### A. Intrinsic Flood Histogram

27  $\times$  27 distinct crystals were resolved from the 2-D flood histogram (see Fig. 2). Examining the energy spectrum of the edge crystals, there is a dual photopeak caused by two edge crystals mapping to same location on the PSPMT. It is possible to resolve an extra row of crystals through the use of energy gating. However, edge crystals were not used because they had significantly degraded energy resolution which caused hot edge artifacts from the phantom injection site activity (Fig. 1). The poor energy resolution at the edge could accept back-scatter photons

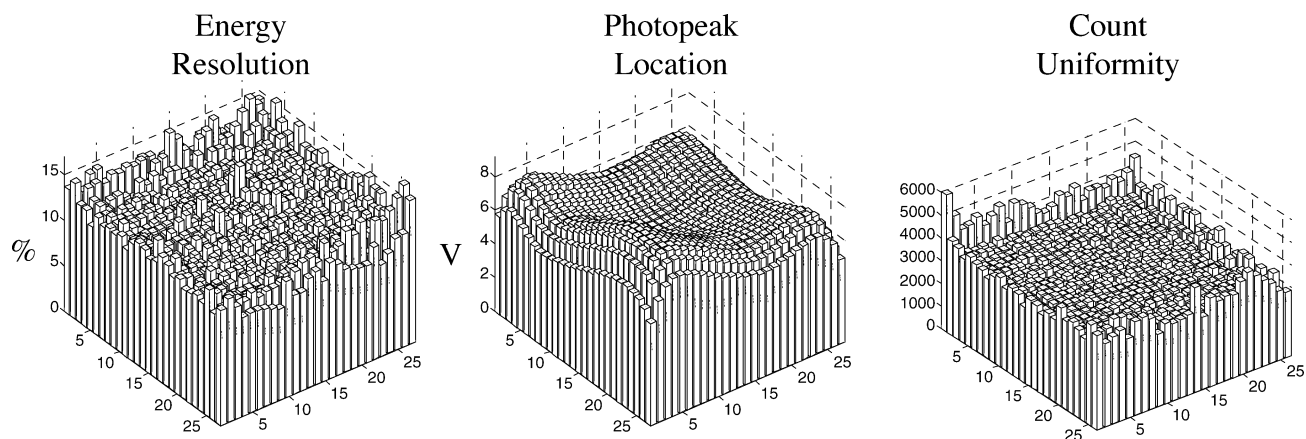


Fig. 3. Individual crystal statistics for the NaI(Tl) array acquired with Tc-99m flood source and a parallel-hole collimator. The individual crystals were segmented from the flood image using a minimum distance to peak classifier. After events are binned to individual crystals, a two Gaussian fit is performed to find the main photopeak location (**middle**), and % energy resolution (**left**). After energy resolution is calculated,  $2 \times$  FWHM energy gating per crystal is performed to create the final intrinsic flood 2-D histogram and the count rate uniformity map (**right**). The photopeak location has a maximum 2:1 variation due to photocathode non-uniformity of the PSPMT.

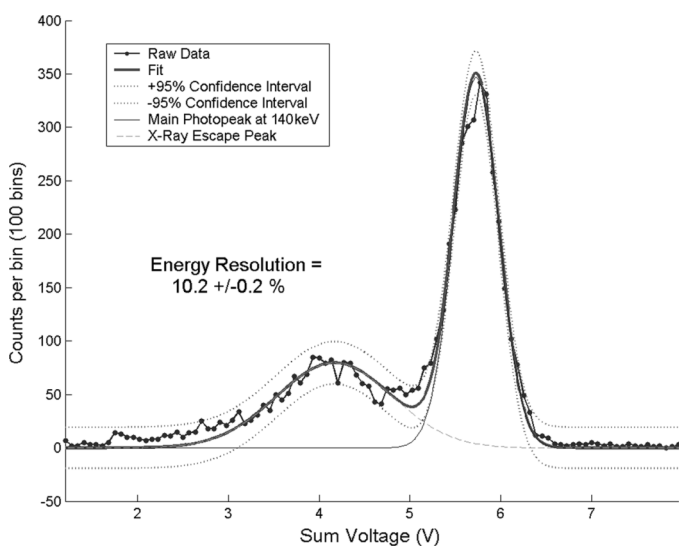


Fig. 4. Best flood energy spectrum measured for a crystal in the center of the array acquired with Tc-99m 140 keV photons.

and lead x-rays to cause hot edge artifacts even when a narrow energy window is used.

### B. Energy Resolution

The NaI(Tl) crystal array has a good average energy resolution of  $13.2 \pm 2.2\%$  and  $12.1 \pm 2.0\%$  for the Co-57 photopeak at 122 keV and Tc-99m at 140 keV, respectively (see Figs. 3 and 4), including the edge crystals averaged over the inner  $27 \times 27$  (out of a total of  $29 \times 29$ ) crystals. For the inner  $25 \times 25$  crystals, the average energy resolution is  $11.6 \pm 0.6\%$  for Tc-99m at 140 keV. Some of the corner crystals have energy resolution  $>15\%$ , but do not significantly affect the imaging performance. The energy resolution is adequate for one to use a narrow energy window (2 times FWHM) to remove scatter and lead x-ray escape contamination while maintaining high counts.

### C. Intrinsic Spatial Resolution

The intrinsic spatial resolution was measured for 5 crystals that were right of center in the array. The intrinsic spatial resolu-

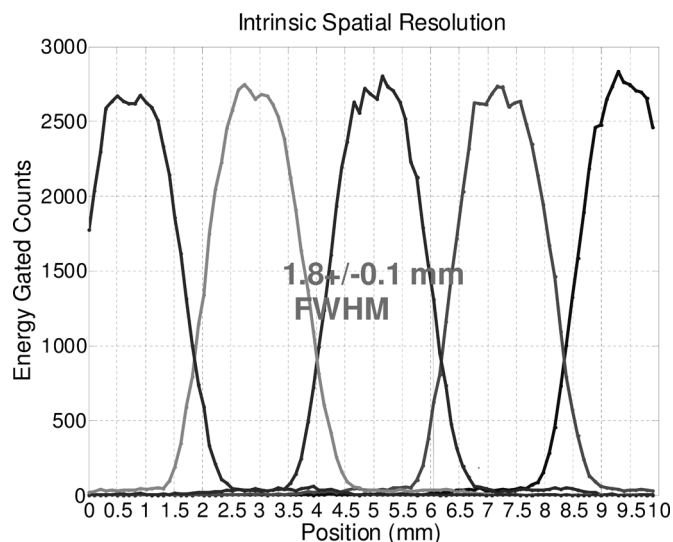


Fig. 5. Intrinsic spatial resolution is measured by stepping a collimated point source across the face of the crystals. The spot size was approximately  $500 \mu\text{m}$ , and the average FWHM of the trapezoid is  $1.8 \pm 0.1 \text{ mm}$ .

tion  $1.8 \pm 0.1 \text{ mm}$  FWHM corresponds well with the  $1.7 \text{ mm}$  pitch of our crystal array (see Fig. 5). Since using a narrow energy gate reduces inter-crystal crosstalk, and the crystals in the flood image are relatively well separated, there is the potential to utilize even smaller crystal sizes than the  $1.5 \text{ mm}$ . However, because of the fixed  $200 \mu\text{m}$  reflector thickness, there would be reduction in sensitivity if we used much smaller than a  $1.5 \text{ mm} \times 1.5 \text{ mm}$  crystal size.

### D. Extrinsic Performance

We studied four different collimator thicknesses and selected the  $20 \text{ mm}$  collimator because it gave the best resolution and sensitivity tradeoff for imaging nodes at  $3 \text{ cm}$  depth (see Fig. 6).

### E. Ideal Observer Using Sphere Phantoms

A planar gamma camera may be considered as a linear projection operator that takes a 3-D source distribution, convolves

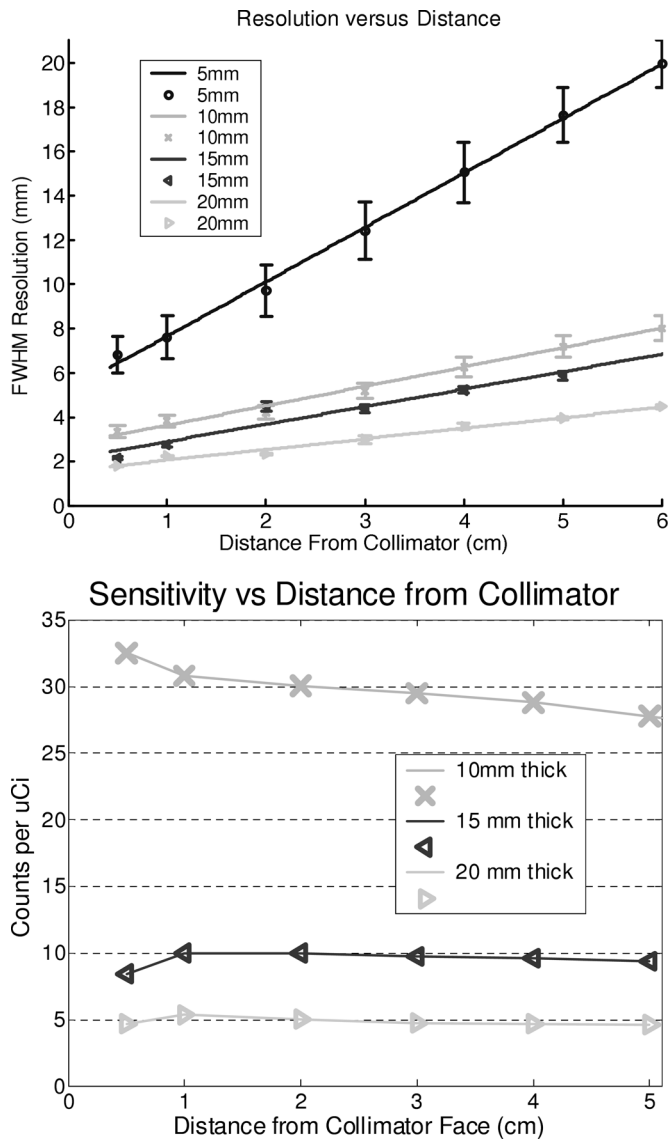


Fig. 6. Resolution and sensitivity as a function of distance for several different collimators of varying thickness. The camera has approximately a 5 cps/ $\mu$ Ci sensitivity and a 1.81  $\pm$  0.1 mm FWHM extrinsic resolution at 0.6 cm for a 20 mm thick collimator.

it with a depth dependant blurring function and projects it onto a 2-D plane. The counts in each pixel recorded by a camera are Poisson distributed, since each pixel is the sum of scaled Poisson distributions (see Fig. 7).

The 3 mm sphere was detectable at 3.6 cm depth in 5 seconds with approximately a 1  $\mu$ Ci total activity in a cold background (see Fig. 8) with a 78  $\pm$  6% true positive probability. In a warm background of 160  $\mu$ Ci total, a 4 mm sphere could be detected at 2.6 cm of depth with 85  $\pm$  1% true positive probability.

**F. Imaging and Image Processing**

We evaluated several image processing algorithms to visualize the real time acquisition at short exposure durations. We found that 3  $\times$  3 Gaussian filtering, bi-cubic image resize  $\times$ 8, and upper 70% adaptive threshold provides (see Fig. 9) optimal image quality for 5 second frames. Exposure duration is an im-

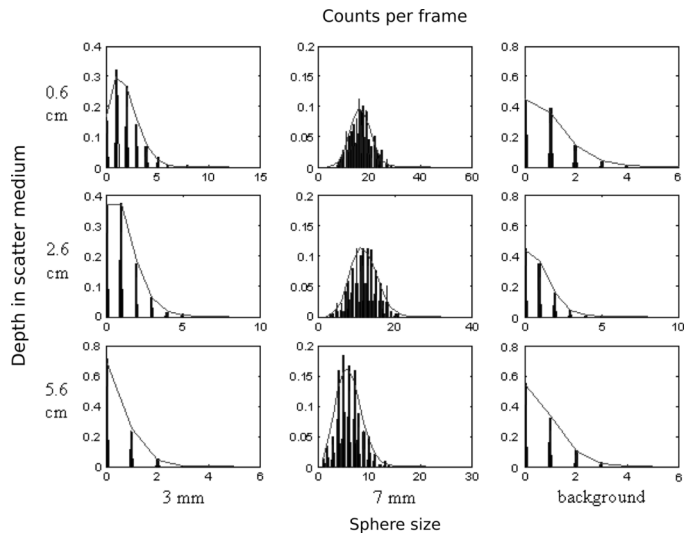


Fig. 7. Extracted counts per frame from 5-second exposure durations. The x-axis of each plot is the number of counts in a region of interest for a selected sphere. The y-axis is the scaled probability. A selected set of statistics from all combinations of different depths (0.6–5.6 cm) and different sphere sizes (3–8 mm) is presented to show how well a Poisson distribution (dark line) fits experimental data (bars). The experimental data are approximately Poisson distributed. Due to resolution effects, depth (0.6 cm versus 5 cm) has a significant effect on the number of events that are detected by the camera.

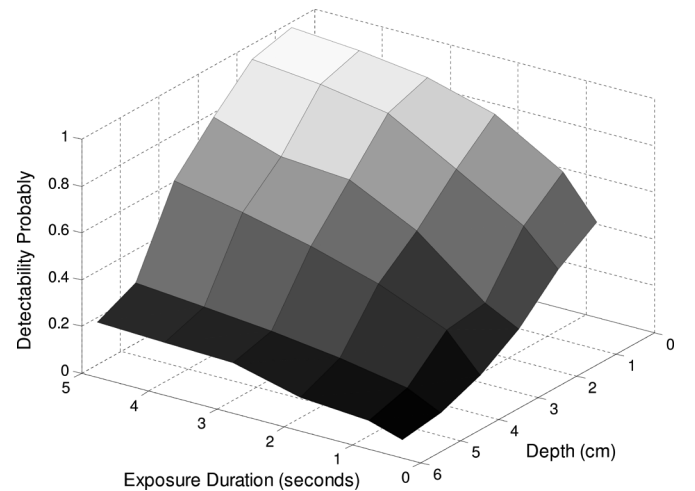


Fig. 8. The detectability of a 3 mm sphere in a cold background as a function of exposure duration and depth in water was calculated using an ideal observer test. The detectability is the probability of detecting signal plus noise minus the probability of detecting noise (positive minus false positive). Longer exposure durations (5 seconds) or shallower depth (0.6 cm) increase the probability of correctly detecting the 3 mm sphere in a frame.

portant factor for detecting small spheres deep within tissue. Although a 5 second acquisition time would be too short for a standard gamma ray camera, Fig. 9 shows that adequate statistics for hot sphere identification is still achieved in 5 seconds using this high sensitivity camera for these realistic activity levels.

**V. DISCUSSION**

We have characterized the intrinsic and extrinsic performance of a small, hand-held gamma camera and quantified certain detectability characteristics using a sphere phantom in a background with a simulated injection site.

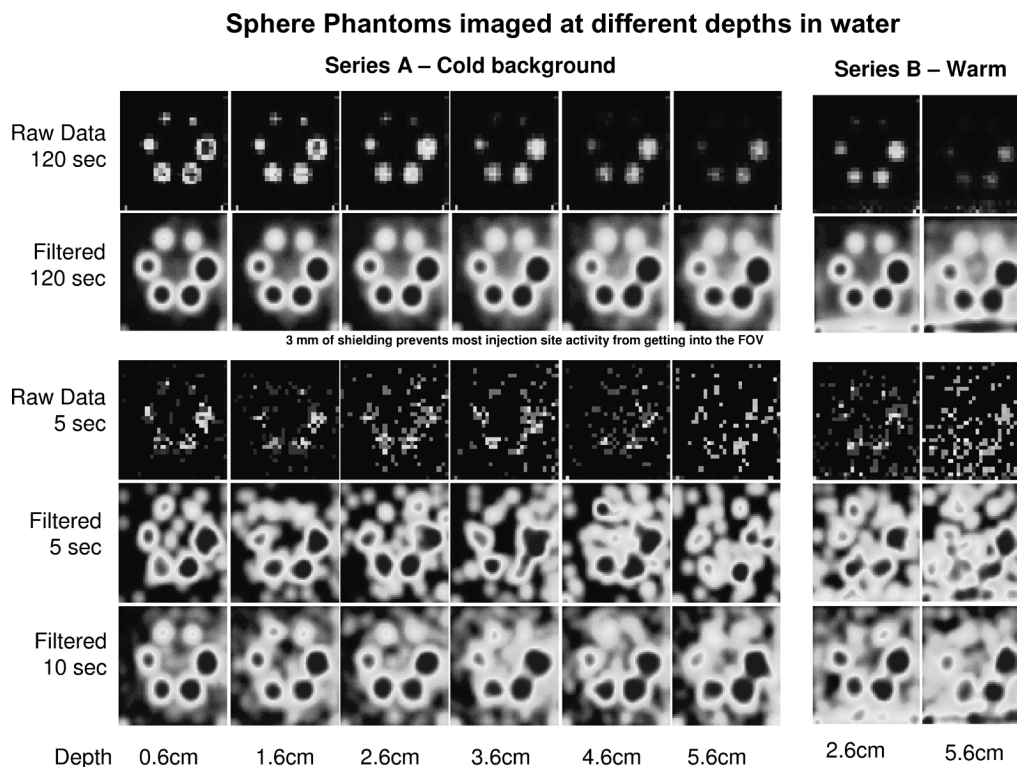


Fig. 9. The sphere phantom is imaged at different depths in water with and without the presence of background (see Fig. 1) using the 20 mm thick collimator. The raw data is shown with a constant intensity scale, while all other frames have an adaptive non-linear intensity scale. The filtering algorithm is a combination of square root compression,  $3 \times 3$  Gaussian filtering, bi-cubic image resize  $\times 8$ , and an adaptive upper 70% threshold. The exposure duration is noted as the number of seconds. High statistics 120-second frames are compared to 5-second and 10-second frames. The simulated injection site ( $250 \mu\text{Ci}$  bottle), which is just out of the field of view, does not significantly contaminate the node phantom image. The amount of activity added to the warm background was  $120 \mu\text{Ci}$  in the 500 mL water tank for the series B acquisitions.

These characterization parameters are important for a simplified task of determining if the camera will work in real-time imaging application attempting to detect small spheres embedded in a scattering medium. We determined that thin collimators have higher sensitivity, but the slope of the spatial resolution as a function of depth is too high to image deep spheres because they become excessively blurred. They provided useful data to test different image processing algorithms, and ideal limits of detectability. We will next examine the utility of this camera in a SLN procedure.

Also, in the proposed hand-held camera application, motion blurring is can be a problem compared to fixed gamma cameras or those that have been attached to an articulating arm [1]. However, fixed gamma cameras do not have the flexibility of hand-held gamma detectors. Another research group has addressed the issue of motion blurring and small field of view of a hand-held camera by attempting to use motion sensors to tile the image into a large synthetic field of view [11], [12]. In this camera, assuming the surgeon scans slowly, the motion blurring can controlled using optical flow [9].

## VI. CONCLUSION

This hand-held scintillation camera has good intrinsic and extrinsic performance. The pixellated scintillation crystal array provides good spatial resolution, sensitivity, and energy resolution. Using an ideal observer, the camera was able to resolve 3

mm diameter spheres with sufficient detectability to pursue further evaluation for sentinel lymph node imaging.

## REFERENCES

- [1] J. N. Aarsvold, R. A. Mintzer, C. Greene, S. F. Grant, T. M. Styblo, D. R. Murray, N. P. Alazraki, R. K. Halkar, L. R. MacDonald, J. S. Iwanczyk, and B. E. Patt, "Gamma cameras for intraoperative localization of sentinel nodes: Technical requirements identified through operating room experience," in *Proc. IEEE Nuclear Science Symp. Conf. Rec.*, Nov. 10–16, 2002, vol. 2, pp. 1172–1176.
- [2] R. F. Uren, R. B. Howman-Giles, J. F. Thompson, D. Malouf, G. Ramsey-Stewart, F. W. Niesche, and S. B. Renwick, "Mammary lymphoscintigraphy in breast cancer," *J. Nucl. Med.*, vol. 36, no. 10, pp. 1775–1780, Oct. 1995.
- [3] N. Alazraki, E. C. Glass, F. Castronovo, R. A. Olmos, and D. Podoloff, "Procedure guideline for lympho-scintigraphy and the use of intraoperative gamma probe for sentinel lymph node localization in melanoma of intermediate thickness 1.0," *J. Nucl. Med.*, vol. 43, no. 10, pp. 1414–1418, Oct. 2002.
- [4] B. A. Kapteijn, O. E. Nieweg, S. H. Muller, I. H. Liem, C. A. Hoefnagel, E. J. Rutgers, and B. B. Kroon, "Validation of gamma probe detection of the sentinel node in melanoma," *J. Nucl. Med.*, vol. 38, no. 3, pp. 362–366, Mar. 1997.
- [5] G. Mariani, L. Moresco, G. Viale, G. Villa, M. Bagnasco, G. Canavese, J. J. Buscombe, H. W. Strauss, and G. Paganelli, "Radioguided sentinel lymph node biopsy in breast cancer surgery," *J. Nucl. Med.*, vol. 42, no. 8, pp. 1198–1215, Aug. 2001.
- [6] L. Tafra, "Melanoma vs. breast cancer (abstract)," presented at the 1st Annu. Meeting American Society of Breast Surgeons, Charleston, SC, Apr. 14–15, 2000.
- [7] P. J. Borgstein, R. Pijpers, E. F. Comans, P. J. van Diest, R. P. Boom, and S. Meijer, "Sentinel lymph node biopsy in breast cancer: Guidelines and pitfalls of lymphoscintigraphy and gamma probe detection," *J. Amer. Col. Surg.*, vol. 186, pp. 275–283, 1998.

- [8] P. D. Olcott, J. A. Talcott, C. S. Levin, F. Habte, and A. M. K. Foudray, "Compact readout electronics for position sensitive photomultiplier tubes," *IEEE Trans. Nucl. Sci.*, vol. 52, no. 1, pp. 21–27, Feb. 2005.
- [9] P. D. Olcott and C. S. Levin, "Image processing algorithms to facilitate and enhance sentinel node detection using a hand-held gamma ray camera in surgical breast cancer staging," in *Proc. Workshop Nuclear Radiology of Breast Cancer*, Rome, Italy, Oct. 22–23, 2006.
- [10] W. W. Peterson, T. G. Birdsall, and W. C. Fox, "The theory of signal detectability," *IEEE Trans. Inf. Theory*, vol. 4, no. 4, pp. 171–212, Sep. 1954.
- [11] I. N. Weinberg, V. Zavarzin, R. Pani, and G. De Vincentes, "Implementing reconstruction with hand-held gamma cameras," in *Proc. IEEE Nuclear Science Symp. Conf. Rec.*, Oct. 15–20, 2000, vol. 3, pp. 21/101–21/104.
- [12] I. N. Weinberg, V. Zavarzin, P. Stepanov, D. Beiline, R. Pani, G. DeVincentes, J. C. Zeng, and L. P. Adler, "Flexible geometries for hand-held PET and SPECT cameras," in *Proc. IEEE Nuclear Science Symp Conf. Rec.*, Nov. 4–10, 2001, vol. 2, pp. 1133–1136.